

# CC-Diff: Enhancing Contextual Coherence in Remote Sensing Image Synthesis

Mu Zhang Yunfan Liu\* Yue Liu Hongtian Yu Qixiang Ye

University of Chinese Academy of Sciences, Beijing, China

{zhangmu23, liuyue171, yuhongtian17}@mails.ucas.ac.cn, {liuyunfan, qxye}@ucas.ac.cn

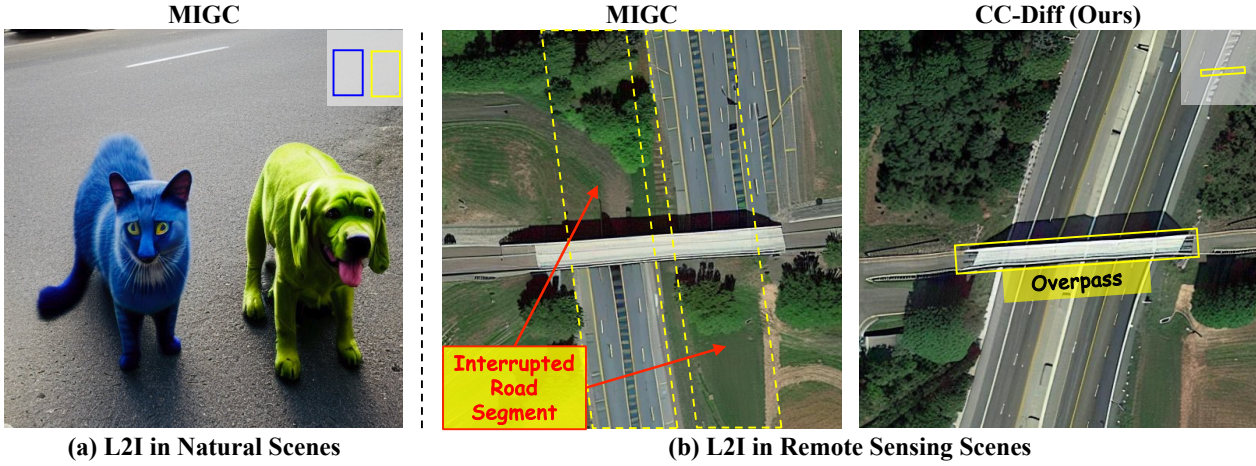


Figure 1. Comparison of Layout-to-Image (L2I) generation for (a) natural images and (b) remote sensing (RS) images (layout shown in the top-right corner). L2I for natural images controls foreground attributes with a simple background, while RS images have complex background textures that are contextually tied to the foreground (e.g., a continuous road passing beneath an overpass).

## Abstract

Accurately depicting real-world landscapes in remote sensing (RS) images requires precise alignment between objects and their environment. However, most existing synthesis methods for natural images prioritize foreground control, often reducing the background to plain textures. This neglects the interaction between foreground and background, which can lead to incoherence in RS scenarios. In this paper, we introduce CC-Diff, a Diffusion Model-based approach for RS image generation with enhanced Context Coherence. To capture spatial interdependence, we propose a sequential pipeline where background generation is conditioned on synthesized foreground instances. Distinct learnable queries are also employed to model both the complex background texture and its semantic relation to the foreground. Extensive experiments demonstrate that CC-Diff outperforms state-of-the-art methods in visual fidelity, semantic accuracy, and positional precision, excelling in both RS and natural image domains. CC-Diff also shows strong trainability, improving detection accuracy by 2.04 mAP on DOTA and 2.25 mAP on the COCO benchmark.

Code is available at <https://github.com/AZZMM/CC-Diff>.

## 1. Introduction

Recent studies have demonstrated the effectiveness of synthetic images in improving the performance of visual perception methods [2, 37, 43, 56]. This promise has motivated growing interest within the Geoscience community to explore remote sensing (RS) image synthesis [12, 36, 39, 49, 53], which has the potential to enhance the accuracy on various analytical tasks, e.g., oriented object detection [15, 40, 51] and landscape segmentation [3, 21, 41].

Despite remarkable advancements in visual quality, existing RS image generation methods [12, 36, 49] typically rely on text prompts to convey image semantics, which struggle to effectively describe the quantity, position, and orientation of foreground objects. Some studies tackle this issue by incorporating dense guidance information (e.g., semantic maps) to improve controllability [39, 53], but this inevitably increases annotation costs and limits the flexibility and diversity of the generated results.

Motivated by recent advances in controlled image gener-

\*Corresponding Author

ation, the Layout-to-Image (L2I) synthesis technique offers a promising solution to the aforementioned problem. However, existing L2I methods [16, 47, 57–59] primarily focus on ensuring the fidelity of foreground attributes concerning conditional information (e.g., texture, color, position) while overlooking their contextual alignment with the background (see Figure 1). This oversight may hold less significance in natural image generation, where the background primarily serves as a backdrop (or canvas) for object placement, allowing for minimal interaction between the two. In contrast, this lack of attention can be detrimental in RS images, where objects are closely tied to the semantics of their environment, making contextual coherence essential for generating semantically plausible representations (see Figure 2 for illustration).

To solve this problem, this study introduces CC-Diff, a **Diffusion Model**-based image generation method with enhanced **Context Coherence**. A closer examination of the internal design of current L2I models reveals that the issue likely stems from separate, non-interacting modules for foreground and background synthesis, and this lack of integration results in semantic inconsistencies in the generated images. While CC-Diff uses a multi-branch structure similar to existing methods for synthesizing distinct instances, it innovates by introducing a sequential process where background generation is conditioned on the features of the synthesized foreground elements. To further enhance the realism and coherence of the generated images, CC-Diff employs two sets of learnable queries to explicitly capture both the textural details of the background and its semantic relationship with the foreground instances. Extensive experiments on RS and natural images demonstrate that CC-Diff generates realistic images with high controllability and contextual coherence. Additionally, CC-Diff improves detection accuracy by 2.04 mAP on the popular DOTA dataset [46] in RS studies, and 2.25 mAP on the more generalized COCO benchmark [19], highlighting its strong trainability.

Our contributions are summarized as follows:

- We introduce CC-Diff, an L2I framework designed to improve contextual coherence in generated images, a problem we find crucial for RS images but largely overlooked by most existing methods.
- A novel sequential pipeline is used to model the interdependence between instances and their surroundings, with distinct queries employed to capture both background texture and its relationship with the foreground.
- Experiments demonstrate CC-Diff’s ability to generate realistic and coherent images across both RS and natural domains, which are shown to be effective augmentations for object detection tasks.

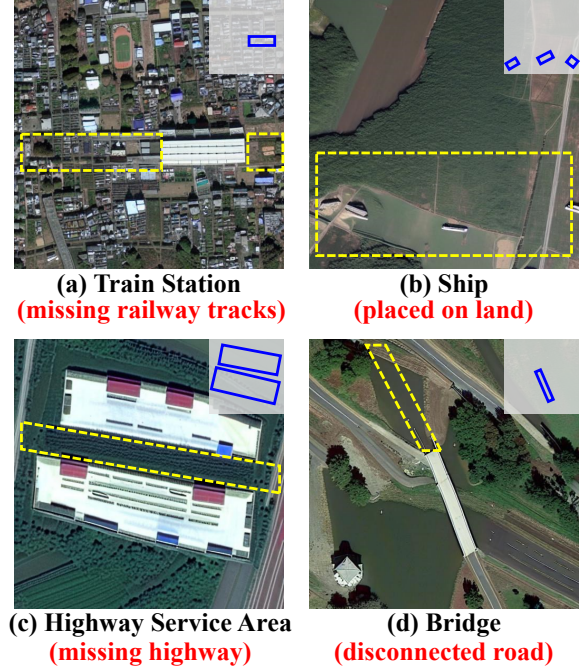


Figure 2. Illustration of contextual incoherencies in RS images synthesized by MIGC [59]. Layouts are shown in the top-right corner, object classes are labeled below, and incoherencies are highlighted with dashed yellow boxes for each figure.

## 2. Related Work

**Controllable Image Generation.** There are two main categories of controllable image generation methods: Text-to-Image (T2I) and Layout-to-Image (L2I), both focused on generating images that correspond to specific input conditions. T2I methods aim to produce images that reflect the semantics of the provided textual descriptions. During the prominence of methods based on Generative Adversarial Network (GAN) [30, 48, 55], DALL-E [28] was among the first to showcase the effectiveness of autoregressive frameworks, with subsequent studies [4, 8, 52] further enhancing fidelity and scalability. A different line of research employs the Diffusion Model [11, 38] alongside text prompts to achieve realistic T2I synthesis [23, 29, 32, 34].

In contrast to T2I, L2I approaches focus on generating images from instance layout to achieve spatial accuracy. With the rise of Diffusion Models, L2I research [16, 42, 47, 50, 57] has increasingly focused on integrating layout conditions into image generation. Recently, Multi-Instance Generation (MIG) in L2I has attracted growing interest [6, 45, 58, 59], with a focus on enhancing foreground instance attributes by separating the generation of foreground elements from background content.

**Remote Sensing Image Synthesis.** While T2I synthesis for natural images has advanced significantly, research in

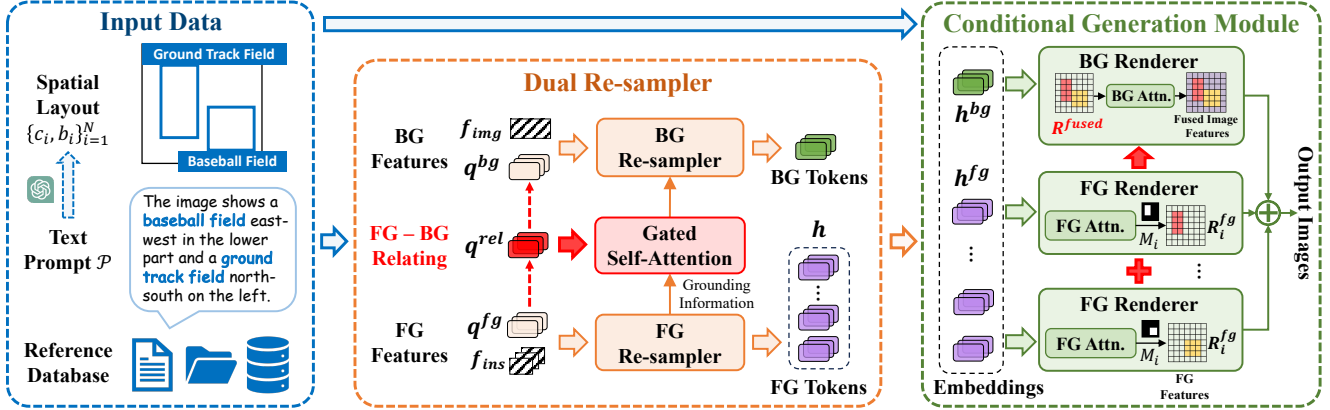


Figure 3. An overview of CC-Diff’s pipeline. The central component of CC-Diff is the **Dual Re-sampler**, which leverages learnable queries to capture detailed features of the foreground ( $q^{fg}$ ), background ( $q^{bg}$ ), and notably their interdependencies ( $q^{rel}$ ). These queries are then passed to the **Conditional Generation Module**, where the background is generated based on the integration of synthesized foreground features ( $R^{fused}$ ), ensuring foreground-awareness throughout the process. Please zoom in for better details.

the RS domain is still in its early stages. Among the initial efforts, Txt2Img-MHN [49] bridges the semantic gap between text prompts and RS images through hierarchical prototype learning. DiffusionSat [12] leverages LDM [33] to generate realistic RS images, controlling semantics through the embeddings of textual descriptions and numeric metadata. RSDiff [36] proposes to introduce a super-resolution network to further enhance image quality. Despite producing visually plausible RS images, these methods struggle to accurately control attributes such as the spatial layout of foreground instances. To address this, recent studies [9, 35, 39, 53] have incorporated additional guiding information, but none focus on ensuring the coherence between foreground and background.

### 3. Preliminaries

#### 3.1. Latent Diffusion Model (LDM)

LDM [32] enhances the computational efficiency of vanilla Diffusion Models [11, 23, 29] by performing denoising in the latent space. After obtaining the latent representation  $\mathbf{z} \in Z$  of the image  $\mathbf{x}$ , LDM seeks to learn a denoising autoencoder  $\epsilon_\theta$ , which progressively generating less noisy data  $\mathbf{z}_{T-1}, \mathbf{z}_{T-2}, \dots, \mathbf{z}_0$  from an initial sampled noise  $\mathbf{z}_T$ . In practice,  $\epsilon_\theta$  is trained to predict the step-wise noise  $\epsilon$  of the forward process, with the objective expressed as

$$\min \mathcal{L}_{LDM} = \mathbb{E}_{\mathbf{z}, \epsilon \sim \mathcal{N}(\mathbf{0}, \mathbf{I}), t} [\|\epsilon - \epsilon_\theta(\mathbf{z}_t, \mathbf{c}, t)\|_2^2] \quad (1)$$

where  $t$  is a time step sampled from interval  $1, \dots, T$  and  $\mathbf{c}$  represents the prompt embedding, enabling semantic controllability via the cross-attention mechanism.

### 3.2. Problem Definition

let  $\mathcal{L} = (\mathcal{P}, \{c_i, b_i\}_{i=1}^N)$  represent the layout containing  $N$  foreground objects, where the  $i$ -th object is annotated by the class label  $c_i$  and positioned by the oriented bounding box  $b_i = [x_i, y_i, w_i, h_i, \alpha_i]$  (i.e., coordinates of the top-left corner  $(x_i, y_i)$ , width  $w_i$ , height  $h_i$ , and orientation angle  $\alpha_i$  (definition detailed in Supp. Mat. Sec 7).  $\mathcal{P}$  serves as an auxiliary textual description of the image’s global semantics (please refer to Supp. Mat. Sec 8 for the detailed construction protocol). In this context, CC-Diff aims to learn a mapping  $\mathcal{G} : (\mathcal{L}, \mathbf{z}) \rightarrow \mathbf{I}$ , where  $\mathbf{I}$  represents the generated image semantically aligned with  $\mathcal{L}$ , and  $\mathbf{z} \sim \mathcal{N}(\mathbf{0}, \mathbf{I})$  is the Gaussian noise.

## 4. Method

### 4.1. Overview

The diagram of the proposed CC-Diff is illustrated in Figure 3. Specifically, CC-Diff employs learnable queries in the **Dual Re-sampler** to explicitly extract semantic information and relationships of key concepts, which are then passed to the **Conditional Generation Module** to guide the synthesis of both foreground instances and the background content. To conceptually implement the sequential pipeline described in Sec. 1, relating queries are utilized to capture the inherent connection between instances and their environment, while feature maps from synthesized foreground objects are fused into the background generation branch to produce an instance-aware background texture. Detailed introduction will be provided in the following subsections.

### 4.2. Associating BG with FG via Relating Query

As highlighted in Sec. 1, the primary distinction between L2I for natural and RS images is the level of textural com-

plexity in the background and the critical role of contextual alignment with foreground instances. Accordingly, unlike most existing L2I approaches that use learnable queries solely to extract features of foreground objects (denoted as  $q^{fg}$ ), we introduce specialized queries to model background texture (background query  $q^{bg}$ ) and to capture the relationship between foreground and background (relating query  $q^{rel}$ ). The queries are learned through the proposed Dual Re-sampler, which will be detailed in the following. **Reference Image Retrieval.** We first briefly describe how reference images are retrieved from the training set. Instances for each foreground category are cropped from training images with SAM[41] to build an exemplar dictionary, from which we randomly sample at generation time as image prompts. For background guidance, we sample one of the top five training images with the highest semantic similarity, computed using CLIP embeddings, as the background reference. Their embeddings are denoted as  $f_{ins}$  and  $f_{img}$ , and please refer to Supp. Mat. Sec 9 for detailed retrieving approach.

**Dual Re-sampler.** As illustrated in Figure 3, the Dual Re-sampler comprises two distinct re-sampler modules for foreground and background (denoted as ‘FG-Resampler’ and ‘BG-Resampler’, respectively), along with an intermediate relating network that models the connection between the two. Both two Re-samplers consist of four consecutive combinations of Cross-Attention (CA) and Feed Forward Network (FFN) layers, where CA enables the interaction between input queries ( $q^{fg}$  and  $q^{bg}$ ) and the embedding of reference images ( $f_{ins}$  and  $f_{img}$ ) retrieved from the training set (further details will be provided later).

Specifically, the token of the  $i$ -th foreground instance (denoted as  $h_i$ ) by the FG-Resampler as follows

$$h_i = \text{FG-Resampler} (q^{fg}, K_i, V_i) \quad (2)$$

where  $K_i, V_i$  ( $i = 1, \dots, N$ ) are projections of  $N$  reference instance embeddings  $f_{ins}$ . In this way, the FG-Resampler serves as an image adapter, querying and extracting relevant features from reference instances to aid in the generation of realistic foreground objects.

To establish the connection between  $q^{fg}$  and  $q^{bg}$ , a set of relating queries ( $q^{rel}$ ) is introduced to capture their contextual information, which is then integrated with  $q^{bg}$  to generate semantically coherent background textures. Specifically,  $q^{rel}$  interacts with the grounded foreground tokens through a Gated Self-Attention (GSA) [16] network, which can be formulated as

$$q^{rel} = q^{rel} + \tanh(\gamma) \cdot (\text{SelfAttn} ([q^{rel}, h^e])) \quad (3)$$

where  $\gamma$  is a learnable scalar and  $h^e = [h_1^e, \dots, h_N^e]$  are grounded foreground tokens obtained through adding the bounding box formation into the output of FG Re-sampler.

Subsequently, only the relating query components of the GSA output encoding the contextual semantics are retained, concatenated with the background query  $q^{bg}$ , and then fed into the BG-Resampler, which can be expressed as

$$h^{bg} = \text{BG-Resampler} ([q^{rel}, q^{bg}], K^{bg}, V^{bg}) \quad (4)$$

where  $K^{bg}, V^{bg}$  are obtained from the embedding of reference image  $f_{img}$ . Similar to the FG-Resampler, the BG-Resampler trains  $q^{bg}$  to extract features from the reference image, while considering the grounded context of the synthesized foreground objects, thereby enhancing the overall coherence of the generated image.

### 4.3. Foreground & Background Generation

**Foreground Instance Synthesis.** As illustrated in Figure 3, the Conditional Generation Module synthesizes each foreground instance via distinctive branches in parallel. The input of each branch, termed foreground embeddings  $h_i^{fg}$ , can be expressed as

$$h_i^{fg} = [h_i, \text{CLIP} (c_i), \text{MLP} (\text{Fourier} (b_i))] \quad (5)$$

which are exactly foreground tokens  $h_i$  concatenated with the embedding of class label  $c_i$  and bounding box  $b_i$ . These input variables control the synthesized foreground instances also via cross-attention, which can be formulated as

$$R_i^{fg} = \text{Softmax} \left( \frac{Q K_i^{fg}{}^T}{\sqrt{d}} \right) V_i^{fg} \cdot M_i \quad (6)$$

where  $K_i^{fg}$  and  $V_i^{fg}$  are projections of the foreground embedding  $h_i^{fg}$  and  $Q$  is computed from the image feature map of the diffusion model backbone. The output of each cross-attention block is then regulated via an instance mask  $M_i$ . Notably, unlike most existing methods adopting binary masks, we resort to a non-uniform implementation using the `Sigmoid()` function, which can be written as

$$\text{Sigmoid} (x, y) = \frac{1}{1 + \exp \left( -1 + \frac{(x - \mu_1)^2}{\sigma_1^2} + \frac{(y - \mu_2)^2}{\sigma_2^2} \right)} \quad (7)$$

where  $\mu_1, \mu_2$  represent the center of the oriented bounding box and  $\sigma_1 = w/2, \sigma_2 = h/2$ . This implementation achieves smooth translation across instances and surrounding texture, as well as a convenient and intuitive representation of oriented objects typically in RS images.

**Conditional Background Generation.** For synthesizing background texture, besides the background queries  $q^{bg}$  encoding the low-level information of reference images, the relating queries  $q^{rel}$  are also involved to introduce contextual knowledge. Moreover, unlike existing approaches where such conditions also interact with the image feature through the cross-attention layer, we propose to straightforwardly reinforce the awareness of foreground features by

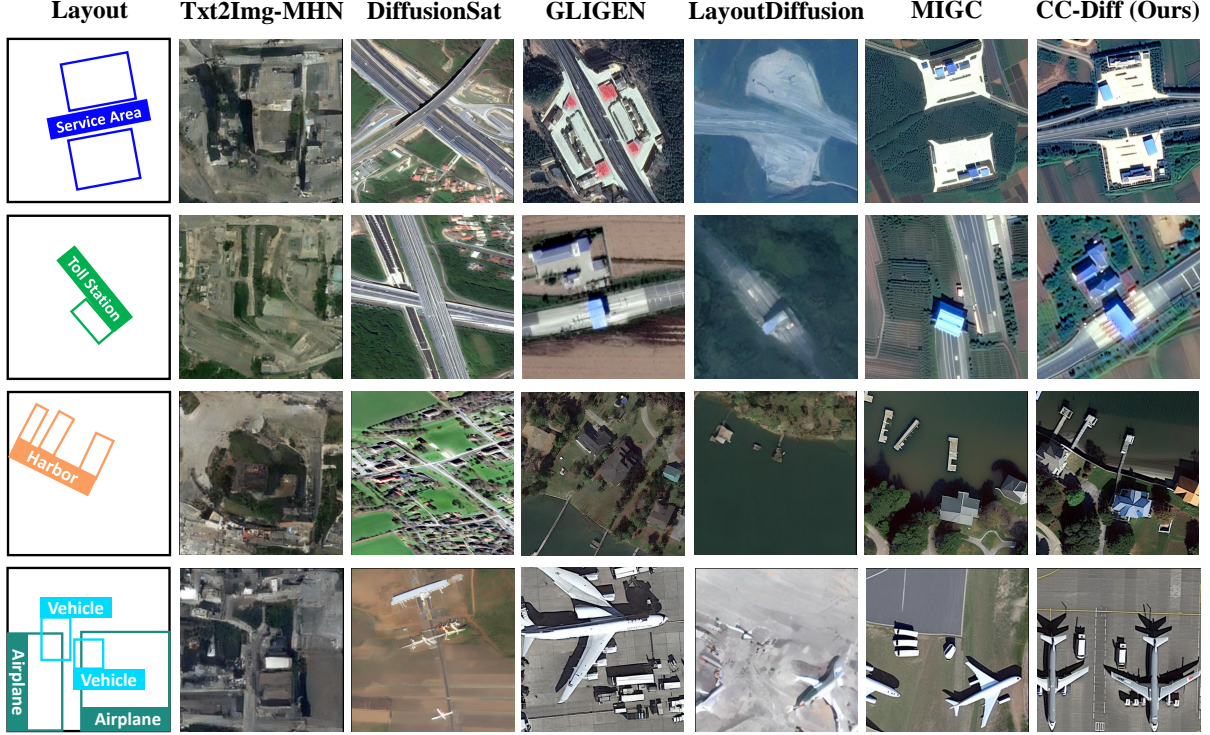


Figure 4. Qualitative L2I results on DIOR-RSVG (top two rows) and DOTA (bottom two rows). CC-Diff not only synthesizes realistic foregrounds with accurate positioning but also generates more detailed backgrounds with stronger coherence to the foreground. Please zoom in for better details.

introducing the fusion of grounded feature maps of all instances, *i.e.*,  $\mathbf{R}^{fused} = \sum_{i=1}^N \mathbf{R}_i^{fg}$ , into the cross-attention mechanism, which can be written as

$$\mathbf{R}^{bg} = \text{Softmax} \left( \frac{Q K^{bgT}}{\sqrt{d}} \right) V^{bg} \quad (8)$$

Similar to the synthesis of foreground instances,  $K^{bg}$  and  $V^{bg}$  are projections obtained from the background embedding  $\mathbf{h}^{bg} = [\mathbf{q}^{bg}, \text{CLIP}(\mathcal{P})]$ , which combines the learned background query  $\mathbf{q}^{bg}$  with the embedding of global semantic  $\mathcal{P}$ . However,  $Q$  is derived from  $\mathbf{R}^{fused}$ , rather than the image feature maps used for foreground synthesis as in Eq 6. In the end, feature maps of foreground and background are added up and sent to the decoder network for producing the final output images.

## 5. Experiments

### 5.1. Experimental Settings

**Datasets.** Following datasets are used in experiments:

- **DIOR-RSVG** [54] comprises 17,402 RS images with a broad spectrum of landscape scales. The number of objects per category is by default restricted to a maximum

of 5, positioning DIOR-RSVG as a controlled baseline for evaluation.

- **DOTA** [46] is a widely used benchmark dataset for RS object detection, containing 2,806 images of varying sizes ranging from 800 to 4,000 pixels. It includes 15 object categories, with no upper limit on the number of objects per image, making DOTA a challenging and practical dataset for our experiments.
- **COCO2017** [19] is a standard benchmark for natural image generation. We employ it to evaluate the generalizability of CC-Diff in handling diverse object categories and complex attributes in natural scenes.

**Implementation Details.** The pre-trained Stable Diffusion V1.4 [32] is used as the backbone for fine-tuning in all experiments. The global text prompt for describing the layout of each image is constructed following the rule-based protocol in [20]. All images are resized to  $512 \times 512$ <sup>1</sup>, with a maximum of 6 objects per image, consistent with recent L2I studies [58, 59]. For all experiments, CC-Diff is trained for 100 epochs with a batch size of 320 on 8  $\times$  NVIDIA A800 GPUs, with a fixed learning rate of  $1e^{-4}$ .

**Benchmark Methods.** We use generation methods from

<sup>1</sup>Images in DOTA are evenly segmented into the same resolution, without considering the integrity of whole objects.

Table 1. Quantitative comparison of results on RS datasets DIOR-RSVG and DOTA. The detector for computing the YOLOScore struggles to detect most instances in images generated by GLIGEN, leading to notably low values (indicated with  $\dagger$ ).

Method	DIOR-RSVG					DOTA				
	CLIPScore $\uparrow$		FID $\downarrow$	YOLOScore $\uparrow$		CLIPScore $\uparrow$	FID $\downarrow$	YOLOScore $\uparrow$		
	Local	Global		mAP <sub>50</sub>	mAP <sub>50-95</sub>			mAP <sub>50</sub>	mAP <sub>50-95</sub>	
Txt2Img-MHN	18.91	23.46	123.84	0.30	0.08	19.58	25.99	137.76	0.02	0.01
DiffusionSat	19.84	<b>32.68</b>	78.16	0.80	0.20	19.78	<b>31.61</b>	65.19	0.04	0.01
GLIGEN	20.55	32.22	73.02	3.44 $\dagger$	0.75 $\dagger$	20.72	29.98	61.05	0.25 $\dagger$	0.07 $\dagger$
LayoutDiffusion	19.31	30.65	79.03	56.92	31.05	20.49	27.67	64.77	28.28	11.40
MIGC	21.59	32.36	79.93	59.55	31.16	22.21	30.96	63.95	35.43	14.85
CC-Diff (Ours)	<b>21.78</b>	32.43	<b>68.03</b>	<b>67.68</b>	<b>41.37</b>	<b>22.42</b>	30.90	<b>47.42</b>	<b>44.54</b>	<b>22.21</b>

Table 2. Trainability ( $\uparrow$ ) comparison on DIOR-RSVG and DOTA. 'Baseline' denotes accuracy with the unaugmented dataset. GLIGEN is excluded due to low detection rates of foreground instances in generated samples.

Method	DIOR-RSVG			DOTA		
	mAP	mAP <sub>50</sub>	mAP <sub>75</sub>	mAP	mAP <sub>50</sub>	mAP <sub>75</sub>
Baseline	50.17	75.84	54.38	35.53	62.10	35.83
Txt2Img-MHN	50.12	75.87	54.74	35.91	62.53	36.43
DiffusionSat	49.95	75.59	55.26	36.15	62.50	36.76
LayoutDiffusion	51.96	77.31	56.82	35.15	61.54	35.18
MIGC	51.87	76.65	57.20	35.93	62.36	36.32
CC-Diff (Ours)	<b>52.62</b>	<b>77.51</b>	<b>58.09</b>	<b>37.57</b>	<b>63.18</b>	<b>38.05</b>

both RS and natural images as benchmarks. Txt2Img-MHN [49] and DiffusionSAT [12] are recent T2I methods for RS images, which are prompted by the previously mentioned rule-based text description. To ensure a fair comparison of spatial controllability and evaluate CC-Diff’s generalizability, we also include state-of-the-art L2I methods for natural image generation: GLIGEN[16], LayoutDiffusion [57], and MIGC [59].

**Evaluation Metrics.** Following [6, 16, 57, 59], we evaluate the performance of CC-Diff across three main aspects:

- **Fidelity:** Synthesis results should appear visually plausible. We use the FID score [10] to evaluate perceptual quality, capturing texture realism and contextual coherence.
- **Faithfulness:** Generated images are expected to align with the provided prompt, with global and local semantic consistency assessed by the Global and Local CLIP-Scores [1]. The YOLOScore [17] computed by an off-the-shelf Faster R-CNN detector [31] further evaluates the alignment of layout for input and output.
- **Trainability:** We examine the potential of considering synthetic images as augmented samples for improving the accuracy of object detection. The standard mean Average Precision (mAP) metric is used for evaluation.

## 5.2. RS Image Synthesis

We start by presenting experimental results on RS datasets, DIOR-RSVG and DOTA. To ensure a fair comparison, we use official checkpoints for all benchmark methods and fine-

tune them on the respective training splits of each dataset.

### 5.2.1. Qualitative Results on RS Datasets

Figure 4 presents a comparison of generated RS images. CC-Diff not only synthesizes realistic foreground instances at varying scales, with accurate positioning and orientation consistent with the given layout, but also generates backgrounds with more intricate textures. More importantly, it establishes a significantly more coherent and plausible relationship between the foreground and background. For example, in the first two cases, CC-Diff successfully renders the road going through the foreground instances, showing a reasonable association with the presence of the expressway service areas and toll station.

As for the benchmark methods, Txt2Img-MHN and DiffusionSat struggle to control the location of foreground objects, despite the inclusion of spatial information in global text prompts. Among the L2I approaches, MIGC achieves the best visual quality and semantic consistency. However, compared to CC-Diff, its rendered background lacks coherence with the foreground, resulting in an implausible landscape. Please refer to Supp. Mat. Sec 10 for more results.

### 5.2.2. Quantitative Results on RS Datasets

Quantitative results on RS datasets are shown in Table 1 and Table 2. In this section, we present a comprehensive analysis from three perspectives including realism, faithfulness, and trainability, as outlined in Sec. 5.1.

**Visual Fidelity.** CC-Diff achieves leading FID scores of 68.03 on DIOR-RSVG and 47.42 on DOTA, outperforming the second-best methods by 10.13 points (DiffusionSat: 78.16) and 16.53 points (MIGC: 63.95), respectively. This clear performance edge can be attributed to CC-Diff’s effective synthesis of realistic instance textures and its enhanced alignment with the overall scene context.

**Semantic Faithfulness.** CC-Diff demonstrates state-of-the-art performance in global and regional semantic alignment, as indicated by CLIPScore values. While Diffusion-Sat achieves a marginally higher Global CLIPScore (32.68 vs. 32.43), this is likely due to its larger RS-specific pre-training dataset [12]. Additionally, CC-Diff shows a clear advantage in YOLOScore, confirming that instances are



Figure 5. Qualitative L2I results on the COCO dataset. In addition to generating realistic foregrounds, CC-Diff produces more plausible and coherent background integration. Please zoom in for better details.

well recognized by the object detector, with accurate layout retention reflected in the high mAP values.

**Trainability.** Following the data enhancement protocol in [6], we double the training samples using layout-based synthesis and assess detection accuracy with the expanded dataset. As shown in Table 2, CC-Diff consistently delivers the highest accuracy gains, improving mAP by 2.45 on DIOR-RSVG and 2.04 on DOTA. Please refer to Supp. Mat. Sec 11 for additional results in fine-grained settings. **To the best of our knowledge, this is the first study to confirm the effectiveness of synthetic samples in improving object detection performance in RS.**

### 5.3. Natural Image Synthesis

#### 5.3.1. Qualitative Results on COCO

The comparison of generation results on the COCO dataset is shown in Figure 5. CC-Diff effectively synthesizes realistic foreground instances and coherent backgrounds, where the semantic connections to the foreground align well with the ground truth. These results demonstrate the strong generalizability of CC-Diff beyond RS image generation.

Table 3. Quantitative comparison of results on COCO.

Method	CLIPScore ↑		FID ↓	YOLOScore ↑	
	Local	Global		mAP <sub>50</sub>	mAP <sub>50-95</sub>
GLIGEN	24.45	30.60	<b>28.69</b>	57.52	35.84
LayoutDiffusion	23.15	21.40	37.26	34.96	17.95
MIGC	24.75	28.84	34.31	<b>59.87</b>	34.64
CC-Diff (Ours)	<b>24.88</b>	<b>31.45</b>	30.35	59.78	<b>36.71</b>

Table 4. Trainability (↑) comparison on COCO. 'Baseline' denotes accuracy with the unaugmented dataset.

Method	mAP	mAP <sub>50</sub>	mAP <sub>75</sub>
Baseline	35.35	59.53	37.50
GLIGEN	37.51	61.18	<b>39.95</b>
LayoutDiffusion	36.39	59.81	38.65
MIGC	37.01	60.45	39.38
CC-Diff (Ours)	<b>37.60</b>	<b>61.44</b>	39.93

#### 5.3.2. Quantitative Results on COCO

We follow the evaluation protocol on RS datasets and assess the performance of CC-Diff on COCO by comparing it to benchmark methods.

Table 5. Ablation on Dual Re-sampler and FG-aware Attention.

Dual Re-sampler	FG-aware Attention	CLIPScore $\uparrow$		FID $\downarrow$	YOLOScore $\uparrow$	
		Local	Global		mAP <sub>50</sub>	mAP <sub>50-95</sub>
$\times$	$\times$	21.69	32.39	72.39	63.85	37.68
$\times$	✓	<b>21.91</b>	32.38	71.17	65.86	39.25
✓	$\times$	21.74	<b>32.43</b>	69.56	64.62	39.22
✓	✓	21.78	<b>32.43</b>	<b>68.03</b>	<b>67.68</b>	<b>41.37</b>

**Visual Fidelity.** As shown in Table 3, CC-Diff achieves an FID score of 30.35 on COCO dataset. Although it is slightly lower than the seminal study GLIGEN [16] by 1.66 FID, CC-Diff outperforms MIGC (34.31) by 3.96 and LayoutDiffusion (37.26) by 6.91. This demonstrates the promising generalizability of CC-Diff to natural image datasets with more diverse and complex foreground attributes.

**Semantic Faithfulness.** As indicated by the CLIPScore in Table 3, CC-Diff achieves the best semantic consistency performance at both local and global levels. While MIGC slightly outperforms CC-Diff by 0.09 YOLOScore under mAP50 (59.87 vs 59.78), CC-Diff achieves a more substantial improvement over all benchmarks under mAP50 – 95, demonstrating a stronger ability to preserve layout consistency across a broader range of threshold levels.

**Trainability.** According to Table 4, CC-Diff consistently improves object detection accuracy by incorporating synthetic augmented samples, achieving the largest accuracy gain of 2.25 (from 35.35 to 37.60) under the most comprehensive metric (mAP). This demonstrates that the trainability of synthetic samples generated by CC-Diff can be effectively generalized from RS to natural images.

#### 5.4. Ablation Study

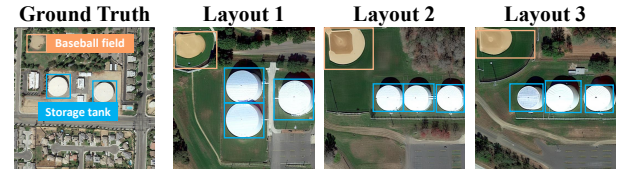
**Sequential Generation Pipeline.** The core innovation of CC-Diff is its sequential generation pipeline, which explicitly models the contextual alignment and semantic interdependence between foreground and background. The *Dual Re-sampler* and *FG-aware Attention* mechanisms are central to this pipeline, and their individual contributions are assessed by omitting each one in turn.

Results shown in Table 5 indicate that integrating the Dual Re-sampler significantly enhances the realism of generated images, with a 1.61 FID score improvement in minimal cases, and also positively impacts the Global CLIPScore (Row 1<sup>st</sup>&2<sup>nd</sup> vs Row 3<sup>rd</sup>&4<sup>th</sup>). Additionally, incorporating foreground-awareness in background generation leads to notable improvements in both YOLOScore and FID (Row 1<sup>st</sup> vs 2<sup>nd</sup>, Row 3<sup>rd</sup> vs 4<sup>th</sup>). These results suggest that contextually coherent backgrounds contribute to enhanced object detection accuracy, as also demonstrated in prior studies [6].

**LLM-assisted T2I.** While synthetic RS images show promising trainability, realistic layout guidance still requires extensive annotation. To address this, we explore

Table 6. ( $\uparrow$ ) performance on DIOR (layout generated with GPT-4o). GLIGEN is excluded due to low detection rates of foreground instances in generated samples.

Method	Trainability			CLIPScore Global	FID
	mAP	mAP <sub>50</sub>	mAP <sub>75</sub>		
Base	50.17	75.84	54.38	31.70	-
Txt2Img-MHN	50.24	75.89	54.86	20.18	184.91
DiffusionSat	49.99	75.49	54.31	32.64	79.33
LayoutDiffusion	50.96	76.46	56.17	30.16	77.48
MIGC	51.35	76.49	56.40	<b>33.13</b>	83.58
CC-Diff (Ours)	<b>51.91</b>	<b>76.80</b>	<b>57.84</b>	32.67	<b>70.61</b>



**Caption:** This is a remote sensing image of storage tanks. There are two storage tanks towards the east-west direction in the center of the image and one storage tank towards the east-west direction in the right edge of the image. There is one baseball field towards the east-west direction in the upper-left corner of the image.



Figure 6. Illustration of various layouts generated by GPT-4 from the same rule-based caption (shown below), along with the corresponding images synthesized by CC-Diff.

using Large Language Models (LLMs) to generate plausible foreground layouts from the same rule-based textual descriptions [20] that prompted Txt2Img-MHN and DiffusionSat in previous experiments (Sec. 5.2).

As shown in Table 6, CC-Diff improves overall detection accuracy by 1.74 mAP and consistently achieves the highest performance gains across all trainability settings. Additionally, CC-Diff demonstrates strong global semantic consistency, reflected by a Global CLIPScore comparable to Ground Truth and an FID score that surpasses the second-best method by 6.87 points (77.48 to 70.61). Furthermore, Figure 6 demonstrates CC-Diff’s adaptability to LLM-generated layout conditions, showcasing its promising zero-shot capability and the diversity of this LLM-based T2I pipeline.

## 6. Conclusion

Existing image generation methods often overlook the coherence between foreground and background, yet this is crucial for generating plausible RS images. To address this, we propose CC-Diff, an L2I method that focuses on rendering intricate background textures while ensuring a context-

tually coherent connection to foreground instances. By employing a sequential generation pipeline, CC-Diff conceptually models the interdependence of foreground and background, utilizing specific queries to capture fine-grained background features and their relationships. Experimental results confirm that CC-Diff can generate visually plausible images across both RS and natural domains, which also exhibit promising trainability on object detection.

## References

[1] Omri Avrahami, Thomas Hayes, Oran Gafni, Sonal Gupta, Yaniv Taigman, Devi Parikh, Dani Lischinski, Ohad Fried, and Xi Yin. Spatext: Spatio-textual representation for controllable image generation. In *CVPR*, pages 18370–18380, 2023. 6

[2] Bahar Aydemir, Deblina Bhattacharjee, Tong Zhang, Mathieu Salzmann, and Sabine Süsstrunk. Data augmentation via latent diffusion for saliency prediction. In *ECCV*, pages 360–377, 2025. 1

[3] Benedikt Blumenstiel, Johannes Jakubik, Hilde Kühne, and Michael Vössing. What a mess: Multi-domain evaluation of zero-shot semantic segmentation. *NeurIPS*, 36, 2024. 1

[4] Huiwen Chang, Han Zhang, Jarred Barber, Aaron Maschinot, José Lezama, Lu Jiang, Ming-Hsuan Yang, Kevin Patrick Murphy, William T. Freeman, Michael Rubinstein, Yuanzhen Li, and Dilip Krishnan. Muse: Text-to-image generation via masked generative transformers. pages 4055–4075, 2023. 2

[5] Keyan Chen, Bowen Chen, Chenyang Liu, Wenyuan Li, Zhengxia Zou, and Zhenwei Shi. Rsmamba: Remote sensing image classification with state space model. *TGRS Letters*, 21:1–5, 2024. 1

[6] Kai Chen, Enze Xie, Zhe Chen, Yibo Wang, Lanqing Hong, Zhenguo Li, and Dit-Yan Yeung. Geodiffusion: Text-prompted geometric control for object detection data generation. In *ICLR*, 2024. 2, 6, 7, 8

[7] Jaemin Cho, Abhay Zala, and Mohit Bansal. Visual programming for step-by-step text-to-image generation and evaluation. *NeurIPS*, 36, 2023. 2

[8] Ming Ding, Zhuoyi Yang, Wenyi Hong, Wendi Zheng, Chang Zhou, Da Yin, Junyang Lin, Xu Zou, Zhou Shao, Hongxia Yang, et al. Cogview: Mastering text-to-image generation via transformers. *NeurIPS*, 34:19822–19835, 2021. 2

[9] Miguel Espinosa and Elliot J. Crowley. Generate your own scotland: Satellite image generation conditioned on maps. *NeurIPS 2023 Workshop on Diffusion Models*, 2023. 3

[10] Martin Heusel, Hubert Ramsauer, Thomas Unterthiner, Bernhard Nessler, and Sepp Hochreiter. Gans trained by a two time-scale update rule converge to a local nash equilibrium. *NeurIPS*, 30, 2017. 6

[11] Jonathan Ho, Ajay Jain, and Pieter Abbeel. Denoising diffusion probabilistic models. *NeurIPS*, 33:6840–6851, 2020. 2, 3

[12] Samar Khanna, Patrick Liu, Linqi Zhou, Chenlin Meng, Robin Rombach, Marshall Burke, David B. Lobell, and Stefano Ermon. Diffusionsat: A generative foundation model for satellite imagery. In *ICLR*, 2024. 1, 3, 6

[13] Alexander Kirillov, Eric Mintun, Nikhila Ravi, Hanzi Mao, Chloe Rolland, Laura Gustafson, Tete Xiao, Spencer Whitehead, Alexander C Berg, Wan-Yen Lo, et al. Segment anything. In *ICCV*, pages 4015–4026, 2023. 2

[14] Soyeong Kwon, Taegyeong Lee, and Taehwan Kim. Zero-shot text-guided infinite image synthesis with llm guidance. *arXiv preprint arXiv:2407.12642*, 2024. 2

[15] Yuxuan Li, Qibin Hou, Zhaohui Zheng, Ming-Ming Cheng, Jian Yang, and Xiang Li. Large selective kernel network for remote sensing object detection. In *ICCV*, pages 16794–16805, 2023. 1

[16] Yuheng Li, Haotian Liu, Qingyang Wu, Fangzhou Mu, Jianwei Yang, Jianfeng Gao, Chunyuan Li, and Yong Jae Lee. Glichen: Open-set grounded text-to-image generation. In *CVPR*, pages 22511–22521, 2023. 2, 4, 6, 8

[17] Zejian Li, Jingyu Wu, Immanuel Koh, Yongchuan Tang, and Lingyun Sun. Image synthesis from layout with locality-aware mask adaption. In *ICCV*, pages 13819–13828, 2021. 6

[18] Long Lian, Boyi Li, Adam Yala, and Trevor Darrell. Llm-grounded diffusion: Enhancing prompt understanding of text-to-image diffusion models with large language models. 2024, 2024. 2

[19] Tsung-Yi Lin, Michael Maire, Serge Belongie, James Hays, Pietro Perona, Deva Ramanan, Piotr Dollár, and C Lawrence Zitnick. Microsoft coco: Common objects in context. In *ECCV*, pages 740–755, 2014. 2, 5

[20] Fan Liu, Delong Chen, Zhangqinyun Guan, Xiaocong Zhou, Jiale Zhu, Qiaolin Ye, Liyong Fu, and Jun Zhou. Remoteclip: A vision language foundation model for remote sensing. *IEEE TGRS*, 62:1–16, 2024. 5, 8, 1

[21] Yinhe Liu, Sunan Shi, Junjue Wang, and Yanfei Zhong. Seeing beyond the patch: Scale-adaptive semantic segmentation of high-resolution remote sensing imagery based on reinforcement learning. In *ICCV*, pages 16868–16878, 2023. 1

[22] Xiaoqiang Lu, Binqiang Wang, Xiangtao Zheng, and Xuelong Li. Exploring models and data for remote sensing image caption generation. *IEEE TGRS*, 56(4):2183–2195, 2017. 1

[23] Alexander Quinn Nichol, Prafulla Dhariwal, Aditya Ramesh, Pranav Shyam, Pamela Mishkin, Bob McGrew, Ilya Sutskever, and Mark Chen. GLIDE: towards photorealistic image generation and editing with text-guided diffusion models. pages 16784–16804, 2022. 2, 3

[24] OpenAI. Chatgpt. <https://openai.com/chatgpt/>, 2024. Accessed: 2024-11-21. 2

[25] Quynh Phung, Songwei Ge, and Jia-Bin Huang. Grounded text-to-image synthesis with attention refocusing. In *CVPR*, pages 7932–7942, 2024. 2

[26] Leigang Qu, Shengqiong Wu, Hao Fei, Liqiang Nie, and Tat-Seng Chua. Layoutllm-t2i: Eliciting layout guidance from llm for text-to-image generation. In *ACM MM*, pages 643–654, 2023. 2

[27] Alec Radford, Jong Wook Kim, Chris Hallacy, Aditya Ramesh, Gabriel Goh, Sandhini Agarwal, Girish Sastry,

Amanda Askell, Pamela Mishkin, Jack Clark, et al. Learning transferable visual models from natural language supervision. pages 8748–8763, 2021. 2

[28] Aditya Ramesh, Mikhail Pavlov, Gabriel Goh, Scott Gray, Chelsea Voss, Alec Radford, Mark Chen, and Ilya Sutskever. Zero-shot text-to-image generation. pages 8821–8831, 2021. 2

[29] Aditya Ramesh, Prafulla Dhariwal, Alex Nichol, Casey Chu, and Mark Chen. Hierarchical text-conditional image generation with clip latents. *arXiv preprint arXiv:2204.06125*, 2022. 2, 3

[30] Scott Reed, Zeynep Akata, Xinchen Yan, Lajanugen Logeswaran, Bernt Schiele, and Honglak Lee. Generative adversarial text to image synthesis. pages 1060–1069, 2016. 2

[31] Shaoqing Ren, Kaiming He, Ross Girshick, and Jian Sun. Faster r-cnn: Towards real-time object detection with region proposal networks. 39(6):1137–1149, 2016. 6

[32] Robin Rombach, Andreas Blattmann, Dominik Lorenz, Patrick Esser, and Björn Ommer. High-resolution image synthesis with latent diffusion models. In *CVPR*, pages 10684–10695, 2022. 2, 3, 5

[33] Robin Rombach, Andreas Blattmann, Dominik Lorenz, Patrick Esser, and Björn Ommer. High-resolution image synthesis with latent diffusion models. In *CVPR*, pages 10684–10695, 2022. 3

[34] Chitwan Saharia, William Chan, Saurabh Saxena, Lala Li, Jay Whang, Emily L Denton, Kamyar Ghasemipour, Raphael Gontijo Lopes, Burcu Karagol Ayan, Tim Salimans, et al. Photorealistic text-to-image diffusion models with deep language understanding. *NeurIPS*, 35:36479–36494, 2022. 2

[35] Srikumar Sastry, Subash Khanal, Aayush Dhakal, and Nathan Jacobs. Geosynth: Contextually-aware high-resolution satellite image synthesis. In *CVPR Workshop*, pages 460–470, 2024. 3

[36] Ahmad Sebaq and Mohamed ElHelw. Rsdiff: Remote sensing image generation from text using diffusion model. *Neural Computing and Applications*, pages 1–9, 2024. 1, 3

[37] Krishnakant Singh, Thanush Navaratnam, Jannik Holmer, Simone Schaub-Meyer, and Stefan Roth. Is synthetic data all we need? benchmarking the robustness of models trained with synthetic images. In *CVPR*, pages 2505–2515, 2024. 1

[38] Jascha Sohl-Dickstein, Eric Weiss, Niru Maheswaranathan, and Surya Ganguli. Deep unsupervised learning using nonequilibrium thermodynamics. pages 2256–2265, 2015. 2

[39] Datao Tang, Xiangyong Cao, Xingsong Hou, Zhongyuan Jiang, Junmin Liu, and Deyu Meng. Crs-diff: Controllable remote sensing image generation with diffusion model. *IEEE TGRS*, 62:1–14, 2024. 1, 3

[40] Di Wang, Qiming Zhang, Yufei Xu, Jing Zhang, Bo Du, Dacheng Tao, and Liangpei Zhang. Advancing plain vision transformer toward remote sensing foundation model. *IEEE TGRS*, 61:1–15, 2022. 1

[41] Di Wang, Jing Zhang, Bo Du, Minqiang Xu, Lin Liu, Dacheng Tao, and Liangpei Zhang. Samrs: Scaling-up remote sensing segmentation dataset with segment anything model. *NeurIPS*, 36, 2024. 1, 4

[42] Xudong Wang, Trevor Darrell, Sai Saketh Rambhatla, Rohit Girdhar, and Ishan Misra. Instancediffusion: Instance-level control for image generation. In *CVPR*, pages 6232–6242, 2024. 2

[43] Yifei Wang, Jizhe Zhang, and Yisen Wang. Do generated data always help contrastive learning? In *ICLR*, 2024. 1

[44] Zhenyu Wang, Enze Xie, Aoxue Li, Zhongdao Wang, Xihui Liu, and Zhenguo Li. Divide and conquer: Language models can plan and self-correct for compositional text-to-image generation. *arXiv preprint arXiv:2401.15688*, 2024. 2

[45] Yinwei Wu, Xianpan Zhou, Bing Ma, Xuefeng Su, Kai Ma, and Xinchao Wang. Ifadapter: Instance feature control for grounded text-to-image generation. *arXiv preprint arXiv:2409.08240*, 2024. 2

[46] Gui-Song Xia, Xiang Bai, Jian Ding, Zhen Zhu, Serge Beßongie, Jiebo Luo, Mihai Datcu, Marcello Pelillo, and Liangpei Zhang. Dota: A large-scale dataset for object detection in aerial images. In *CVPR*, 2018. 2, 5

[47] Jinheng Xie, Yuexiang Li, Yawen Huang, Haozhe Liu, Wentian Zhang, Yefeng Zheng, and Mike Zheng Shou. Boxdiff: Text-to-image synthesis with training-free box-constrained diffusion. In *ICCV*, pages 7452–7461, 2023. 2

[48] Tao Xu, Pengchuan Zhang, Qiuyuan Huang, Han Zhang, Zhe Gan, Xiaolei Huang, and Xiaodong He. Attngan: Fine-grained text to image generation with attentional generative adversarial networks. In *CVPR*, pages 1316–1324, 2018. 2

[49] Yonghao Xu, Weikang Yu, Pedram Ghamisi, Michael Kopp, and Sepp Hochreiter. Txt2img-mhn: Remote sensing image generation from text using modern hopfield networks. *IEEE TIP*, 32:5737–5750, 2023. 1, 3, 6

[50] Zhengyuan Yang, Jianfeng Wang, Zhe Gan, Linjie Li, Kevin Lin, Chenfei Wu, Nan Duan, Zicheng Liu, Ce Liu, Michael Zeng, et al. Reco: Region-controlled text-to-image generation. In *CVPR*, pages 14246–14255, 2023. 2

[51] Hongtian Yu, Yunjie Tian, Qixiang Ye, and Yunfan Liu. Spatial transform decoupling for oriented object detection. *AAAI*, 38(7):6782–6790, 2024. 1

[52] Jiahui Yu, Yuanzhong Xu, Jing Yu Koh, Thang Luong, Gunjan Baid, Zirui Wang, Vijay Vasudevan, Alexander Ku, Yinfei Yang, Burcu Karagol Ayan, Ben Hutchinson, Wei Han, Zarana Parekh, Xin Li, Han Zhang, Jason Baldridge, and Yonghui Wu. Scaling autoregressive models for content-rich text-to-image generation. 2022, 2022. 2

[53] Zhiqiang Yuan, Chongyang Hao, Ruixue Zhou, Jialiang Chen, Miao Yu, Wenkai Zhang, Hongqi Wang, and Xian Sun. Efficient and controllable remote sensing fake sample generation based on diffusion model. *IEEE TGRS*, 61:1–12, 2023. 1, 3

[54] Yang Zhan, Zhitong Xiong, and Yuan Yuan. Rsvg: Exploring data and models for visual grounding on remote sensing data. *IEEE TGRS*, 61:1–13, 2023. 5

[55] Han Zhang, Jing Yu Koh, Jason Baldridge, Honglak Lee, and Yinfei Yang. Cross-modal contrastive learning for text-to-image generation. In *CVPR*, pages 833–842, 2021. 2

[56] Shiyu Zhao, Long Zhao, Yumin Suh, Dimitris N Metaxas, Manmohan Chandraker, Samuel Schulter, et al. Generating enhanced negatives for training language-based object detectors. In *CVPR*, pages 13592–13602, 2024. 1

- [57] Guangcong Zheng, Xianpan Zhou, Xuewei Li, Zhongang Qi, Ying Shan, and Xi Li. Layoutdiffusion: Controllable diffusion model for layout-to-image generation. In *CVPR*, pages 22490–22499, 2023. [2](#), [6](#)
- [58] Dewei Zhou, You Li, Fan Ma, Zongxin Yang, and Yi Yang. Mige++: Advanced multi-instance generation controller for image synthesis. *arXiv preprint arXiv:2407.02329*, 2024. [2](#), [5](#)
- [59] Dewei Zhou, You Li, Fan Ma, Xiaoting Zhang, and Yi Yang. Mige: Multi-instance generation controller for text-to-image synthesis. In *CVPR*, pages 6818–6828, 2024. [2](#), [5](#), [6](#)

# CC-Diff: Enhancing Contextual Coherence in Remote Sensing Image Synthesis

## Supplementary Material

Due to space constraints in the main submission, we provide the detailed implementation and explanation of the proposed CC-Diff in this Supplementary Material. Specifically, we present the implementation details of CC-Diff, including the definition of the bounding box orientation, the rule-based protocol for constructing the global text prompt  $\mathcal{P}$ , the procedure for retrieving reference images for foreground and background synthesis from the dataset, and the specification of CC-Diff’s internal structure. Additionally, we include further experimental results to underscore the effectiveness of CC-Diff.

### 7. Definition of the Bounding Box Orientation

Unlike natural images, where horizontal bounding boxes (HBB) are commonly used to delineate object contours, RS images require additional angular information to capture object orientation. This necessitates the use of oriented bounding boxes (OBB), which extend HBB by incorporating a rotation angle (as shown in Figure 7 (a)).

Given the existence of multiple conventions for defining the angular component of OBBs, we adopt the ‘long edge 90° (le90)’ definition throughout this study. Under this convention, an OBB is represented as  $(x, y, w, h, \theta)$ , where  $(x, y)$  indicates the bounding box’s center,  $w$  and  $h$  correspond to width and height of the box, and  $\theta$  specifies the angle of rotation.

Specifically, the angle  $\theta$  is measured between the longer edge of the bounding box and the positive x-axis, with clockwise rotations taken as positive and counterclockwise as negative (see Figure 7 (b) and (c)). This angle is confined to the range  $[-90^\circ, 90^\circ]$  in degrees, which, in our experiments, is expressed in radians as  $[-\pi/2, \pi/2]$ .

### 8. Construction of the Global Text Description and the GPT Prompt

**Global Text Description.** The captions employed in recent Text-to-Image synthesis methods for remote sensing (RS) (e.g., Txt2Img-MHN [49] and DiffusionSat [12]) primarily describe the quantity and categories of foreground objects, often neglecting their spatial arrangement within the RS image. To address this limitation and incorporate spatial guidance into the text prompt, we adopt a rule-based protocol from [20] to generate artificial descriptions, denoted as  $\mathcal{P}$  in the main submission, that capture the spatial semantics of the scene.

As shown in Figure 8, to efficiently incorporate spatial information into the text, this method divides the RS image into  $K \times K$  blocks ( $K = 4$  for the example in Figure 8),

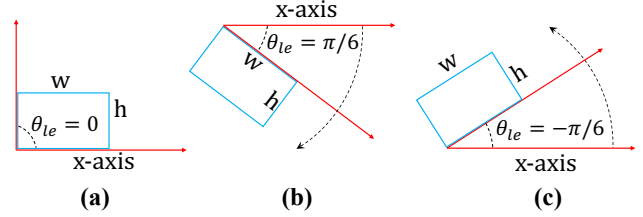


Figure 7. Definition of oriented bounding box (OBB) angles.

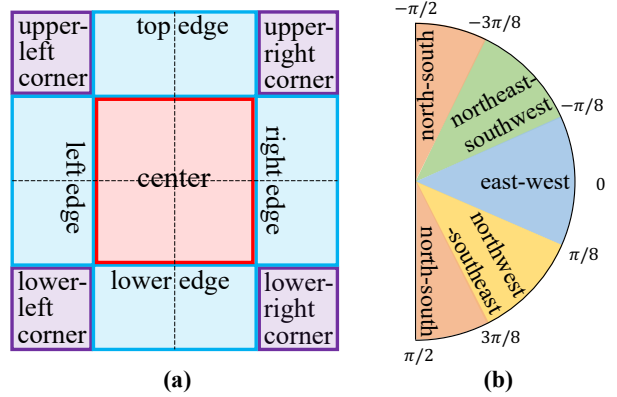


Figure 8. Illustration of (a) image space division and (b) object orientation definition for global textual description construction.

defining the  $\lfloor K/2 \rfloor \times \lfloor K/2 \rfloor$  blocks at the center of the image as the ‘central region’. The remaining blocks are named based on their relative positions to the central region (e.g., ‘upper’, ‘lower-right’, etc.). Following [22], the text description for a single image is constructed as follows:

1. The first sentence offers a general description of the RS image to be generated. It follows the template: ‘This is a remote sensing/an aerial image of <img\_cls>.’, where <img\_cls> represents the class label of the RS image, obtained using the open-source classification model presented in [5].
2. Objects with their centers located in the central region are described first, with the class prioritized by descending instance count. The description for each type of foreground object follows the template: ‘There is/are <obj\_num> of <obj\_cls> towards the <obj\_ori> direction in <obj\_pos>.’ Here, <obj\_num> represents the number of instances, <obj\_cls> specifies the object class, <obj\_ori> indicates the orientation, and <obj\_pos> denotes the block-level location within the image.
3. For objects located outside the central region, the same

template and prioritization are applied.

4. The total number of sentences in the prompt is capped at 5, with any remaining objects excluded from the description.

Please refer to the sample captions shown in Figure 6 of the main submission, which serve as the global text descriptions used across all experiments.

**GPT Prompt.** We use GPT-4o [24] as the LLM for layout planning based on the given text prompt. Inspired by the practice in [7, 14, 18, 25, 26, 44], the prompt consists of two main sections: Instruction and Context Examples. In the Instruction section, we specify the task setting, constraints, and GPT’s role. This includes details about the OBB format and the definition and significance of each of its components. For the Context Examples, captions and layout pairs are retrieved using a reference image retrieval approach, selecting five samples with high semantic similarity to the query text description. These captions and layouts are incorporated into the prompt to define the expected input-output relationship for GPT, without including the original images themselves. We provide an example of the GPT prompt as follows.

The instruction section of prompt mainly contains following parts:

1. Task setting:

You are an intelligent research assistant. I will provide the caption of an aerial image captured by a satellite. Your task is to:

- (a) Identify the object categories mentioned in the caption.
- (b) Count the number of instances for each category.
- (c) Generate an oriented bounding box (OBB) for each instance in the format: (object name, [center x, center y, width, height, rotation angle]).

2. Constraints:

- Image size is 512x512, with the top-left at [0, 0] and the bottom-right at [512, 512].
- The width must always be greater than the height.
- The rotation angle is the angle between the longer edge (width) and the positive x-axis, measured in degrees within [-90, 90].
- Bounding boxes must stay entirely within the image boundaries.
- Do not include objects not mentioned in the caption.

### 3. GPT’s role:

Validate that all bounding boxes meet the width  $>$  height and boundary conditions. If necessary, make reasonable assumptions for object layout based on common aerial imagery.

Please refer to the example below for the desired output format.

We select the five examples with the highest similarity to the given caption as the in-context examples. An example is shown as follows:

Example #1:

<Input Caption>

This is an aerial image of airplane. There are three airplanes, two towards the northwest-southeast direction, one towards the northeast-southwest direction in the center of the image.

<Output Bounding Boxes>

airplane: [247, 221, 121, 112, 30]

airplane: [306, 357, 110, 105, 33]

airplane: [207, 336, 120, 112, -36]

## 9. Reference Image Retrieval

To improve the visual quality of synthesized results, we employ a method inspired by augmented image retrieval [], selecting reference images from the training set based on specific criteria to supply dense guiding information. The detailed procedure is outlined as follows:

1. We use SAM [13] to segment instances from patches cropped from training images based on HBB annotations. For each category, the segmented instances are sorted by resolution (in descending order), and the top-ranked ones (e.g., 200) are selected to build a reference dictionary. During inference, a reference instance, whose embedding is denoted as  $f_{ins}$  in the main submission, is randomly chosen from the dictionary based on the querying class label.
2. For the background reference image with embedding  $f_{img}$ , we select the one that is semantically closest to the construction image caption  $\mathcal{P}$  (described in Sec 8). To improve efficiency, we pre-compute and store the CLIP embeddings of the training images [27]. During retrieval, we compute the similarity between the CLIP embedding of  $\mathcal{P}$  and the stored embeddings, then randomly sample one of the top five images with the highest similarity values as  $f_{img}$ .

Figure 9 provides an illustration of the retrieved instances and reference images for further reference.

**Ablation on Reference Image Guidance.** We also assess the impact of integrating reference images retrieved from the training set. As shown in Table 7, using reference images for foreground synthesis notably improves the FID by 3.6 points (from 75.46 to 71.86) and slightly enhances the Local CLIPScore. Meanwhile, incorporating background reference images primarily contributes to higher YOLOScores and further improvements in FID.

## 10. Additional Qualitative Results

Extra generation results on RS dataset and COCO are presented in Figure 11 and Figure 12, respectively.

## 11. Trainability AP

The detailed trainability results are provided in Tables 8, 9, and 10, where the accuracy improvements for each individual object class are presented to facilitate a more thorough analysis.

From Table 8, it is evident that CC-Diff outperforms across multiple categories, particularly in complex and diverse scenarios. It achieves the highest scores in categories such as golf field (54.19), stadium (75.10), train station (28.87), harbor (12.26), storage tank (80.57), airport (47.57), and dam (36.40). These results underscore CC-Diff’s strong generalization capabilities and its effectiveness in handling a variety of scenarios within the DIOR-RSVG dataset, demonstrating its potential for remote sensing image analysis. This ability is further reflected in the DIOR dataset with layout prompts generated by GPT-4o (Table 9) and the DOTA dataset for RS object detection (Table 10).

Table 7. Ablation on reference, † indicates random sampling.

FG	BG	CLIPScore $\uparrow$		YOLOScore $\uparrow$	
		Local	Global	FID $\downarrow$	mAP <sub>50</sub>
✗	✗	21.76	32.42	75.46	66.20
✗	✓	21.70	<b>32.58</b>	71.90	67.10
✓	✗	21.80	32.32	71.86	65.30
✓	✓ <sup>†</sup>	<b>21.81</b>	32.43	70.00	67.35
✓	✓	21.78	32.43	<b>68.03</b>	<b>67.68</b>
					<b>41.37</b>

## 12. Detailed Implementation of CC-Diff

**Dual Re-sampler** As illustrated in Figure 9, Both BG-Resampler and FG-Resampler consist of four consecutive combinations of Cross-Attention (CA) and Feed Forward Network (FFN) layers. The CA layers in FG-Resampler enable the interaction between foreground queries ( $q^{fg}$ ) and the embedding of foreground instances ( $f_{ins}$ ) retrieved from the training set and then extract the foreground tokens ( $h$ ). To establish the connection between  $q^{fg}$  and  $q^{bg}$ , relating queries ( $q^{rel}$ ) first interact with the grounded foreground tokens obtained through adding the bounding box formation into the foreground tokens through a GSA network and

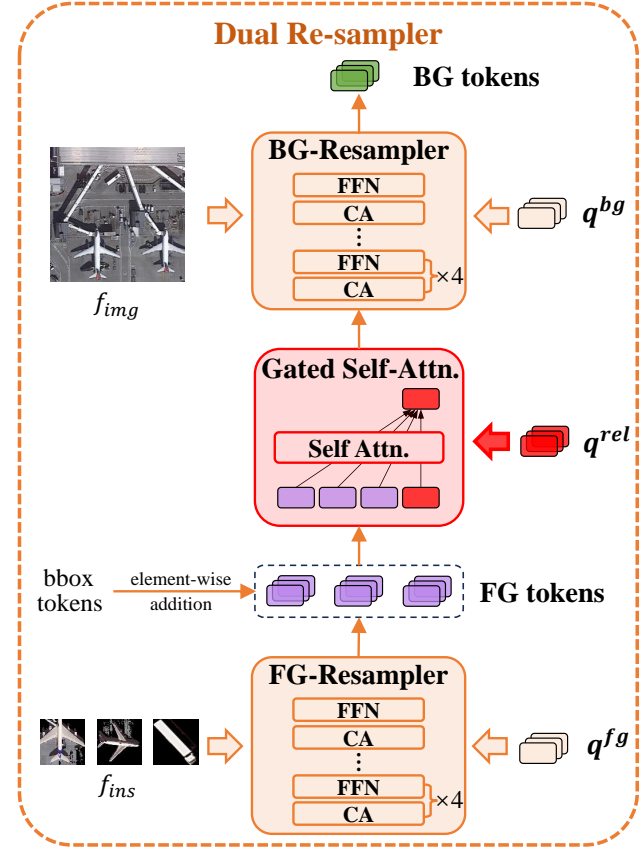


Figure 9. Detailed Dual Re-sampler Structure

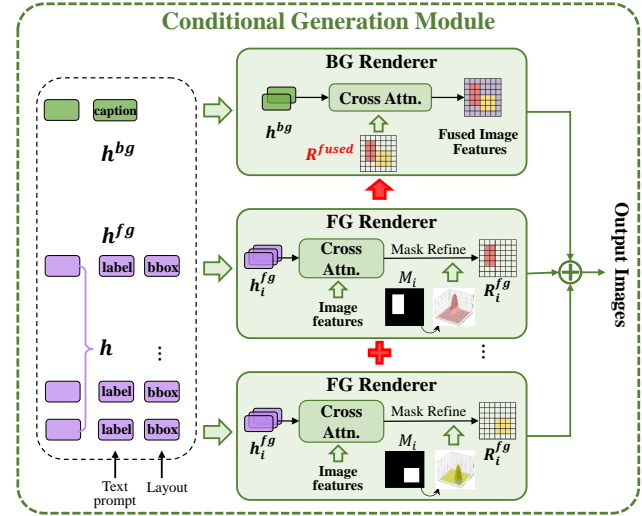


Figure 10. Detailed Conditional Generation Module Structure

then concatenate with  $q^{bg}$ . The combination results, together with the embedding of reference image ( $f_{img}$ ) are finally fed into the CA layers in BG-Resampler to obtain background tokens with overall coherence of the generated

image.

**Conditional Generation Module** As illustrated in Figure 10, the Conditional Generation Module synthesizes each foreground instance via distinctive branches in parallel. The input of each branch, termed foreground embeddings  $h_i^{fg}$  are foreground tokens  $h_i$  concatenated with the embedding of class label  $c_i$  and bounding box  $b_i$ . Specifically, a grounding MLP consisting of a Fourier Transform and a MLP network is utilized to encode  $b_i$  into a positional embedding, and we use the CLIP text encoder to compute the embedding of the text description. These input variables control the synthesized foreground instances also via cross-attention, where the foreground embeddings  $h^{fg}$  interact with the image feature map of the diffusion model backbone. The output of each cross-attention block is then regulated via an instance mask  $M_i$  which is implemented using the Sigmoid Function and then obtain the foreground features  $R_i^{fg}$ .

Similar to foreground instances, the generation of background is controlled by the background embeddings ( $q^{bg}$ ) which combine the background tokens with the embedding of global semantic  $\mathcal{P}$ . Moreover, we straightforwardly reinforce the awareness of foreground features by introducing the fusion of grounded feature maps of all instances, *i.e.*,  $R^{fused} = \sum_{i=1}^N R_i^{fg}$ , into the cross-attention mechanism to obtain background feature maps. In the end, feature maps of foreground and background are added up and sent to the decoder network for producing the final output images.

Table 8. Detailed trainability results (measured by average precision) on DIOR-RSVG.

Method	vehicle	chimney	golf field	Expressway-toll-station	stadium	ground track field	windmill	train station	harbor	overpass
Baseline	43.50	70.07	48.16	56.43	70.95	68.32	51.34	22.57	7.76	36.91
Txt2Img-MHN	<b>43.61</b>	67.67	45.73	55.06	71.44	68.70	51.30	23.87	9.52	38.25
DiffusionSat	43.43	67.76	47.94	55.61	69.94	68.06	51.47	23.12	6.85	36.84
LayoutDiffusion	42.68	68.50	50.39	<b>57.69</b>	73.30	<b>69.57</b>	<b>52.38</b>	28.23	9.20	<b>40.33</b>
MIGC	43.38	<b>70.39</b>	53.58	55.50	72.15	69.52	50.79	25.93	10.34	39.52
CC-Diff (Ours)	42.66	69.44	<b>54.19</b>	57.07	<b>75.10</b>	69.50	51.31	<b>28.87</b>	<b>12.26</b>	39.51

Method	baseball field	tennis court	bridge	basketball court	airplane	ship	storage tank	Expressway-Service-area	airport	dam
Baseline	76.81	<b>54.63</b>	25.97	54.05	68.18	51.77	80.22	42.15	44.17	29.38
Txt2Img-MHN	76.73	51.81	27.51	54.45	69.41	50.90	79.95	43.80	41.06	31.56
DiffusionSat	76.34	54.31	27.23	53.59	69.21	51.35	79.27	43.54	41.86	31.30
LayoutDiffusion	<b>76.83</b>	54.34	<b>30.36</b>	54.67	68.97	53.54	79.34	<b>49.94</b>	46.85	32.05
MIGC	76.76	54.09	28.94	<b>56.68</b>	<b>70.05</b>	52.91	<b>80.57</b>	46.22	<b>47.57</b>	32.51
CC-Diff (Ours)	76.35	54.58	28.59	56.43	69.37	<b>54.91</b>	79.92	49.45	46.58	<b>36.40</b>

Table 9. Detailed trainability results (measured by average precision) on the DIOR dataset (layout generated using GPT-4o).

Method	vehicle	chimney	golf field	Expressway-toll-station	stadium	ground track field	windmill	train station	harbor	overpass
Baseline	43.50	70.07	48.16	56.43	70.95	68.32	51.34	22.57	7.76	36.91
Txt2Img-MHN	43.54	68.77	46.71	<b>56.67</b>	71.49	69.06	50.73	24.00	8.91	37.21
DiffusionSat	<b>43.65</b>	68.95	44.92	55.60	70.86	68.47	51.34	23.82	8.94	37.92
LayoutDiffusion	42.91	67.57	49.34	55.06	73.24	68.74	<b>52.43</b>	<b>25.86</b>	6.22	<b>38.13</b>
MIGC	41.84	70.28	52.76	55.93	73.34	<b>69.95</b>	51.54	24.00	9.16	37.14
CC-Diff (Ours)	42.82	<b>71.46</b>	<b>56.93</b>	54.74	<b>73.93</b>	68.92	50.95	24.75	<b>10.03</b>	38.06

Method	baseball field	tennis court	bridge	basketball court	airplane	ship	storage tank	Expressway-Service-area	airport	dam
Baseline	<b>76.81</b>	54.63	25.97	54.05	68.18	51.77	80.22	42.15	44.17	29.38
Txt2Img-MHN	76.72	52.88	26.88	53.06	<b>70.06</b>	50.92	<b>80.27</b>	45.59	41.27	30.03
DiffusionSat	76.15	55.22	26.13	54.64	69.08	51.32	79.24	41.76	43.00	28.72
LayoutDiffusion	76.39	56.06	<b>29.66</b>	55.71	68.70	51.71	79.13	47.54	44.93	29.88
MIGC	75.50	55.34	27.86	56.75	69.72	<b>52.07</b>	79.70	45.11	46.09	<b>32.99</b>
CC-Diff (Ours)	76.23	<b>56.13</b>	27.78	<b>57.48</b>	68.09	51.79	79.37	<b>49.03</b>	<b>47.85</b>	31.85

Table 10. Detailed trainability results (measured by average precision) on DOTA.

Method	plane	ship	storage-tank	baseball-diamond	tennis-court	basketball-court	ground-track-field
Baseline	50.68	31.73	30.01	36.16	77.95	34.21	41.80
Txt2Img-MHN	50.31	32.64	30.90	36.16	77.84	34.32	44.23
DiffusionSat	50.63	32.23	30.92	<b>36.55</b>	78.12	36.79	41.41
LayoutDiffusion	49.67	31.55	29.67	36.16	78.22	34.38	41.40
MIGC	49.65	31.58	31.04	35.37	78.25	38.01	44.22
CC-Diff (Ours)	<b>51.82</b>	<b>35.90</b>	<b>31.09</b>	35.73	<b>81.42</b>	<b>43.46</b>	<b>44.34</b>

Method	harbor	bridge	large-vehicle	small-vehicle	helicopter	roundabout	soccer-ball-field	swimming-pool
Baseline	38.63	24.13	26.99	24.64	25.86	33.64	38.67	17.94
Txt2Img-MHN	38.72	23.76	27.60	23.56	28.08	32.85	38.94	18.69
DiffusionSat	38.87	24.25	<b>27.95</b>	23.96	<b>29.74</b>	<b>33.99</b>	39.12	17.67
LayoutDiffusion	38.38	25.27	25.90	24.42	25.78	31.51	38.10	16.83
MIGC	38.33	23.49	25.63	24.27	27.39	32.41	40.55	18.72
CC-Diff (Ours)	<b>40.29</b>	<b>25.42</b>	27.57	<b>25.44</b>	25.60	33.52	<b>41.72</b>	<b>20.30</b>



Figure 11. Additional qualitative results are presented for DIOR-RSVG and DOTA. The first three rows highlight CC-Diff’s ability to generate detailed backgrounds that exhibit strong coherence with the foreground. The middle three rows showcase its capability to synthesize images with complex backgrounds, while the last three rows demonstrate its effectiveness in generating scenes with multiple instances.

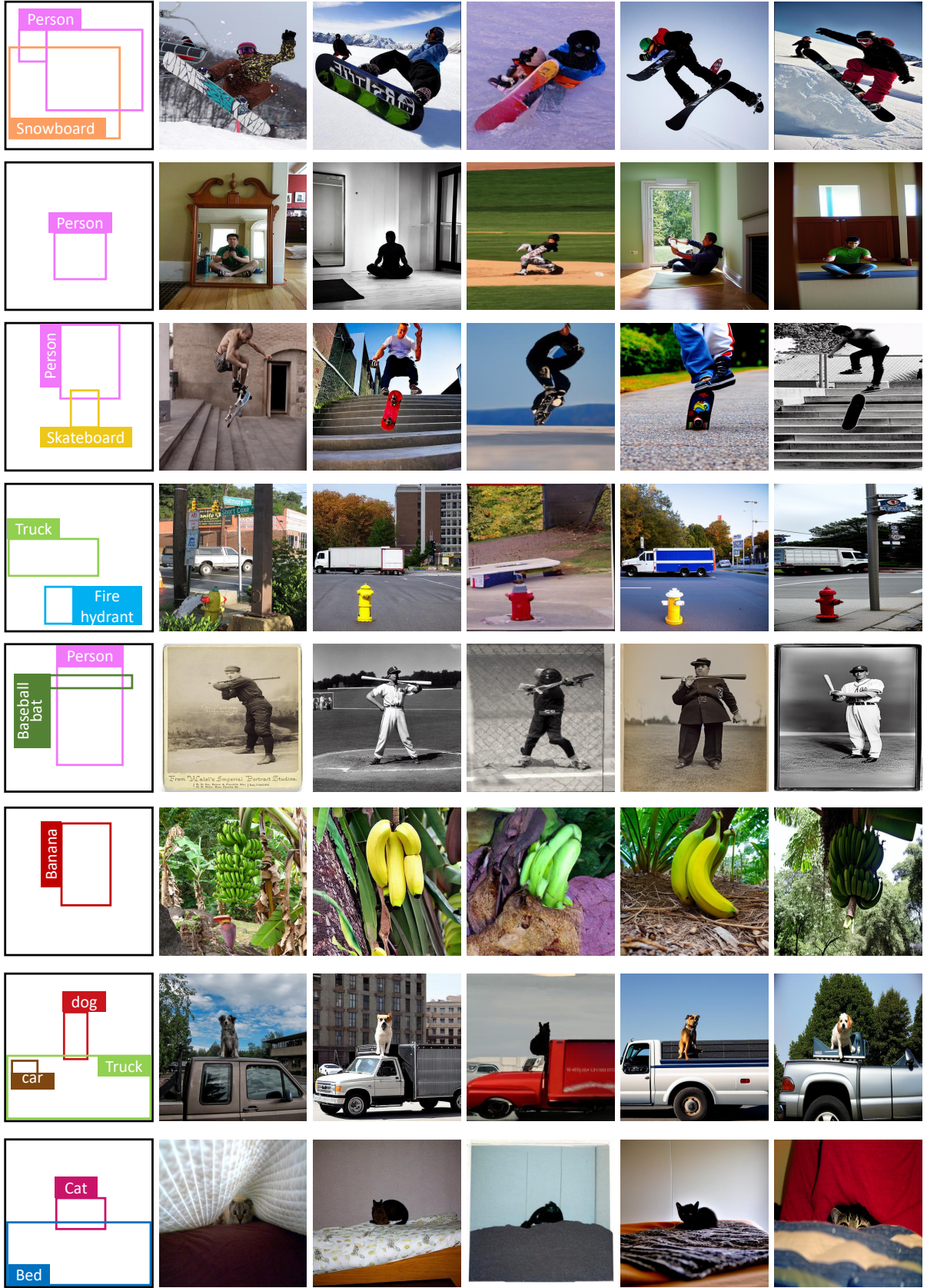


Figure 12. Additional qualitative results on COCO. Beyond generating realistic foreground instances, CC-Diff demonstrates enhanced coherence and establishes more plausible relationships between the foreground and background.